RSC Advances

PAPER

View Article Online
View Journal | View Issue

Cite this: *RSC Adv.*, 2023, **13**, 6108

Adsorption of crystal violet on activated bamboo fiber powder from water: preparation, characterization, kinetics and isotherms

Shushuang Sun,[ab] Yaming Zhu, *[a] Zishuo Gu,[a] Hongyu Chu,[a] Chaoshuai Hu,[a] Lijuan Gao[a] and Xuefei Zhao*[a]

Biomass-activated carbon has made a great contribution as an adsorbent in the field of dye wastewater treatment. In this study, the response surface method (RSM) based on the Box–Behnken design was used to optimize the preparation process. Bamboo fiber activated carbon (BAC) with a specific surface area of 2892 $m^2\ g^{-1}$ and a pore volume of 1.80 $cm^3\ g^{-1}$ was prepared. Various characterization methods (SEM, XPS, XRD, and Raman spectroscopy) were used to analyze the micro-structure of BAC. In the microscopic state, the BAC is fibrous and maintains the originally connected pores of the bamboo fiber. After high-temperature activation, the microcrystallinity of BAC decreases, and the degree of graphitization is low, indicating the presence of amorphous carbon. The adsorption capacity of BAC to crystal violet in simulated wastewater was evaluated *via* an adsorption experiment. Under the following conditions: the dosage of BAC was 0.04 g, the concentration was 600 mg L^{-1}, the adsorption temperature and time were 25 °C and 30 min, respectively, and the as-prepared BAC had a 99.96% removal rate. The adsorption process conformed to the pseudo-second-order kinetic model and Langmuir adsorption isotherm model, indicating that the adsorption process of CV on BAC belonged to monomolecular layer adsorption. The adsorption process occurs spontaneously and is accompanied by heat release, and the maximum adsorption capacity of BAC within a given concentration range could reach 1353.09 mg g^{-1}. SEM-EDS characterization before and after adsorption showed that ion exchange and the presence of oxygen-containing functional groups played an important role in promoting the adsorption process. The results show that BAC considerably affects CV removal, which has great application prospects.

Received 30th December 2022
Accepted 7th February 2023

DOI: 10.1039/d2ra08323j

rsc.li/rsc-advances

1 Introduction

The dye industry is a traditional pillar industry in China, and its processed products are widely used in the textile industry, leather, coating food and cosmetics.[1,2] However, in today's world, with the rapid development of the printing and dyeing textile industry, numerous refractory dyes were discharged into the water body. It was estimated that nearly 800 000 tons of artificial dyes were produced every year, causing serious water pollution.[3,4] Synthetic dyes from water can be eliminated using the membrane separation method, filtration, advanced oxidation method,[5] coagulation and flocculation, and photocatalytic degradation.[6] Laftani *et al.*[7] used the sun-Fenton oxidation process to degrade Lichun red dye in water. The experimental results show that under the degradation conditions of Fe^{2+} concentration of 0.06 mM, H_2O_2 of 1 mM, and initial solution pH of 3, the sun-Fenton oxidation process takes only 10 minutes to degrade dye. The degradation rate was greater than 94.3%. This method is efficient, but it consumes a lot of energy, is expensive, easily causes secondary pollution, and is unsuitable for treating high-concentration dye wastewater. Wang *et al.*[8] prepared a gallic acid-grafted chitosan/polysulfone composite nanofiltration membrane and used it for Congo red dye removal. The results showed that the nanofiltration membrane had a 97.2% rejection rate of Congo red dye, and the flux of the membrane reached 14.0 L $h^{-1}\ m^{-2}\ bar^{-1}$. Membrane separation is efficient, but its life span is short. Aoudjit *et al.*[9] prepared TiO_2-chitosan microspheres (CTCS) for the degradation of tartar dye. The results showed that the degradation rate of tartar dye reached 99.37% in 180 min by synergistic action with CTCS under sunlight. Photocatalytic degradation is a new method, but in the process of degrading dyes, attention must be paid to the problem of transmittance if printing and dyeing wastewater color is deep or too much suspended matter in the water is not conducive to light transmission and affects the photocatalytic effect.[10]

[a]*Institute of Chemical Engineering, University of Science and Technology Liaoning, Anshan 114051, China. E-mail: zhuyaming0504@163.com; zhao_xuefei@sohu.com*
[b]*School of Energy and Environmental Engineering, University of Science and Technology Beijing, Beijing 100083, China*

The adsorption method has the advantages of low cost, small investment, easy operation and economic benefit, which are widely used in the removal of organic pollutants that are difficult to degrade. The adsorbent used to adsorb pollutants in water usually refers to its large surface area; porous adsorbent or material, activated carbon, bentonite, natural zeolite, silica gel and resin can be used as typical adsorbents to treat dyes in water.[11,12] Maliheh *et al.*[13] used the response surface optimization method to optimize the adsorption conditions of natural zeolite, and under the optimal adsorption conditions, the adsorption capacity of natural zeolite on crystal violet dye reached 177.75 mg g^{-1}. Yu *et al.*[14] prepared biochar by KOH activation and anaerobic pyrolysis with corn cob xylost residue as raw material, showing excellent adsorption performance for Congo red and methyl orange dye, and good recyclability when treating methylene blue solution, with 68.7% adsorption capacity still maintained after 6 cycles. Nowadays, the use of biomass-activated carbon to treat dye wastewater has become a promising and active research field.

In industrial production, crystal violet (CV) is a typical cationic triphenylmethane dye. Synthetic crystal violet has low biodegradability; if it comes in contact with the skin, it causes serious irritation to the skin and eyes, resulting in skin allergy and even cancer.[15,16] Simultaneously, wastewater containing CV dye has a certain toxicity; not controlling its discharge will reduce the light transmittance of water, affect the normal growth of aquatic plants, and cause great damage to the water environment.[17] Nowadays, domestic and foreign researchers with a variety of biomass as raw materials have developed a wide variety of biomass-activated carbon. To better resolve the water pollution crisis and protect the human home, research workers in the process of preparing biomass-activated carbon are in the direction of "high adsorption, high strength, and multi-functional" to prepare materials with a specific-controlled pore structure and function to support the achievement of green energy and zero pollution emission goals. In recent years, much attention has been paid to the search for high-quality biomass to prepare for the high adsorption properties of activated carbon. Bamboo fiber is made from the natural growth of bamboo and has a rich ultra-fine pore structure that exhibits strong adsorption potential. It adheres to the wear resistance and toughness of bamboo and has excellent mechanical properties, a loose porous structure, a hard texture, and a short growth period. The recycling of discarded bamboo fiber is not only conducive to the development of a circular economy and the protection of national energy security but also can achieve the sustainable development of social and environmental protection. Studies have shown that the specific surface area of ordinary bamboo charcoal is 2–3 times that of ordinary charcoal, and one of its most prominent applications is to prepare activated carbon that can be used as a multifunctional adsorbent.[18]

Therefore, bamboo fiber was selected as the precursor of activated carbon preparation in this study; bamboo fiber-activated carbon was prepared, the activated carbon activation process was optimized, and its adsorption performance on the CV was investigated to make the adsorption material achieve an excellent adsorption effect.

2 Experimental

2.1 Raw materials and reagents

The bamboo fibers used in this study are made of bamboo waste from a paper-making industry in Anhui province. Bamboo fibers fermented with CaO were soaked in water for several days, placed in an air-blast dryer, and then crushed with a grinder, followed by sieving using a 200-mesh sieve. Crystal violet ($C_{25}H_{30}N_3Cl$; molecular weight 407.98) and potassium hydroxide (KOH, ≥85%) were procured from the Shenyang Chemical Reagent Factory (Shengyang, China). Absolute ethyl alcohol (CH_3CH_2OH) was purchased from Quanrui Reagent Co., LTD, Jinzhou, China.

2.2 Preparation of bamboo fiber-activated carbon

Bamboo fiber-activated carbon was prepared by employing the KOH activation method. First, bamboo fibers were placed in a tubular furnace and carbonized at 550 °C under N_2 protection for two hours, and the carbonized product was named RC. Then, RC was activated, and the response surface optimization method was used to optimize the activation conditions to obtain bamboo fiber-activated carbon (BAC) with excellent adsorption performance. The synthetic process of bamboo fiber-activated carbon is shown in Fig. 1.

2.3 Design of the experiment

Experimental optimization studies were designed using the Box–Behnken method. Using the iodine adsorption value of bamboo fiber-activated carbon as the response value, process conditions, such as activation temperature, activation time, and alkali/carbon ratio, were investigated at three levels with a range of values shown in Table 1. Design-Expert 10.0.1 software was used to summarize and analyze the adsorption data, and the 3D response surface diagram and contour diagram were used to discuss the interaction between the three factors. Finally, the optimal preparation process parameters for bamboo fiber-activated carbon were obtained.

The main effects and interactions of the variables were obtained by fitting eqn (1). ANOVA is performed on the second-order polynomial equation to judge the significance of the model. The model is deemed capable of predicting the process if the probability P value is less than 0.05:[19,20]

$$y = \beta_0 + \sum_i^k \beta_i x_i + \sum_i^k \beta_{ii} {x_i}^2 + \sum_i \sum_j \beta_{ij} x_i x_j + \varepsilon_e, \quad (1)$$

where y refers to the predicted response value; β_0 is the offset term;β_i, β_{ij}, and β_{ii} refer to the linear effect, interaction effect, and squared effect, respectively;[21] and x_i and x_j are the levels of the independent variables.

According to the response surface experimental results, the bamboo fiber-activated carbon with the highest adsorption performance can be obtained, which is named BAC.

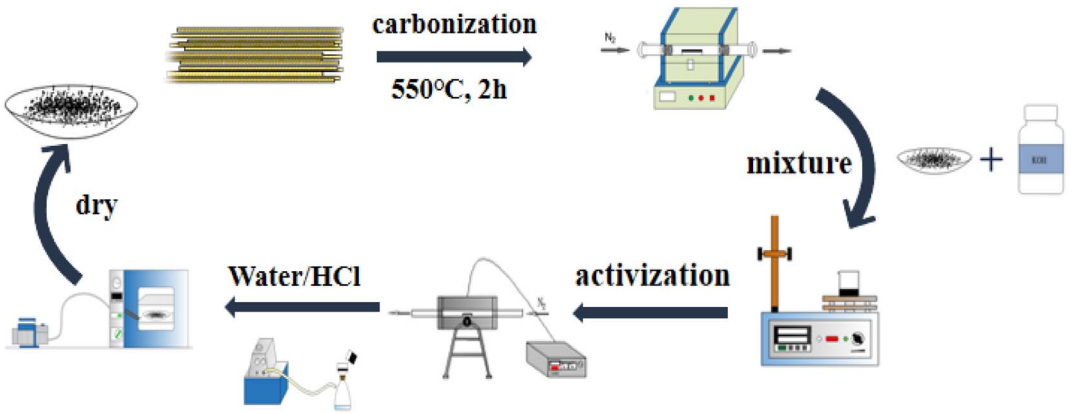

Fig. 1 Flow chart of activated carbon preparation.

Table 1 Response surface factor level design

Notation	*A*: activation temperature/°C	*B*: activation time/min	*C*: alkali/carbon ratio
−1	800	30	4
0	850	45	5
1	900	60	6

2.4 Characterizations of RC and BAC

The elemental analysis of bamboo fiber was tested using an elemental analyzer (Vario ELIII, Elmentar, Germany). The oxygen content was obtained by difference. For industrial analysis, the Industrial Analysis of Solid Biomass Fuel (GB/T 28731-2012) method was adopted. N_2 adsorption/desorption isotherms at 77 K for BAC and RC were obtained using an automatic physical adsorption instrument. The specific surface area and microporous volume were based on the BET method and the *t*-plot model. The surface micro-structure was analyzed using scanning electron microscopy (PIGMA-HD, Germany). The crystal structure was tested using X-ray diffraction and Raman spectroscopy (LabRAM HR Evolution, JOBIN YVON, France). X-ray Photoelectron Spectroscopy (XPS, NY, USA) was applied to further analyze the element types and contents.

2.5 CV adsorption experiments

2.5.1 CV standard working curve drawing. Transfer 1 mL, 2 mL, 3 mL, 5 mL, 6 mL, 8 mL, 9 mL, 10 mL, 12 mL, 15 mL, 20 mL and 25 mL CV standard liquid into 12 50 mL stopper colorimetric tubes with a pipette, fill to 50 mL with deionized water and shake well. The CV standard solution under test was obtained with mass concentrations of 0.2 mg L^{-1}, 0.4 mg L^{-1}, 0.6 mg L^{-1}, 1 mg L^{-1}, 1.2 mg L^{-1}, 1.6 mg L^{-1}, 1.8 mg L^{-1}, 2 mg L^{-1}, 2.4 mg L^{-1}, 3 mg L^{-1}, 4 mg L^{-1} and 5 mg L^{-1}, respectively. The wavelength of the UV-visible spectrophotometer preheated in advance was adjusted to 580 nm, and the absorbance of a series of standard CV solutions was measured with ultra-pure water as the reference. The average value of each

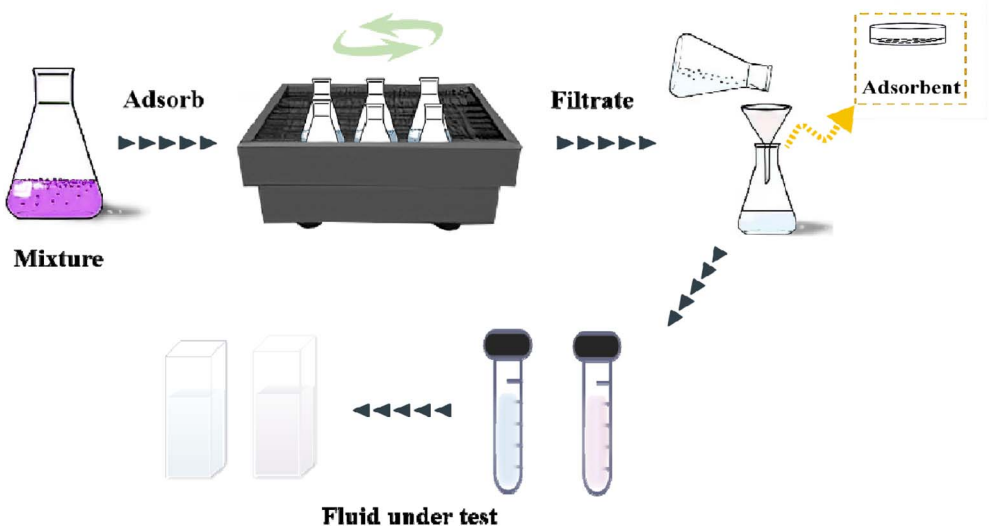

Fig. 2 BAC adsorption crystal violet flow chart.

concentration was measured three times, and the standard curve of the crystal violet concentration and absorbance was drawn.

2.5.2 Batch adsorption experiments for CV. The absorption method is shown in Fig. 2. The effects of three factors that might influence the adsorption process were investigated, including the BAC dosage (0.01 g to 0.06 g), initial dye concentration (400 to 900 mg L^{-1}), and contact time (2 to 40 min). The following formulas were used to calculate the BAC removal rate ω (%) and adsorption capacity q_t (mg g^{-1}) to evaluate the adsorption effect of BAC on CV:

$$\omega = \frac{C_0 - C_t}{C_0} \times 100\%, \quad (2)$$

$$q_t = \frac{V(C_0 - C_t)}{m}, \quad (3)$$

$$q_e = \frac{V(C_0 - C_e)}{m}, \quad (4)$$

where ω (%) is the CV removal efficiency; q_t and q_e are the CV adsorption capacity (mg g^{-1}) at any time t (min) and equilibrium, respectively; C_0, C_t, and C_e are the initial CV concentration, the remaining CV concentration at any time t, and equilibrium CV concentration (mg L^{-1}), respectively; V is the volume of aqueous solution (L); and m is the weight of the BAC used (g).

2.5.3 Adsorption kinetics. Adsorption kinetics were used to understand the mechanism of the adsorption process. The adsorption data were fitted by the pseudo-first order kinetic model (eqn (5)) and pseudo-second order kinetic model (eqn (6)).[22] They can be expressed by the following equations:

$$q_t = q_e(1 - e^{-k_1 t}), \quad (5)$$

$$q_t = \frac{k_2 q_e^2 t}{(1 + k_2 q_e t)}, \quad (6)$$

where t (min) refers to the time during the adsorption process and k_1 and k_2 refer to the adsorption rate constant of the two kinetic models.

2.5.4 Adsorption isotherm. The Langmuir and Freundlich adsorption isotherm models were used to deal with the adsorption data. The Langmuir model is suitable for monolayer adsorption theory, indicating that the adsorption sites on the surface of the adsorbent are uniform, and there is no mutual effect between the adsorbed particles.[23,24] The nonlinear form of the Langmuir isotherm model (eqn (7)) can be defined as follows:

$$q_e = \frac{bq_m C_e}{1 + bC_e}, \quad (7)$$

where q_m represents the saturated adsorption capacity per unit mass and b represents the Langmuir constant related to the adsorption energy.

In the Langmuir equation, the dimensionless separation factor R_L can be used to judge whether the adsorption reaction course is advantageous or not, which can be defined as follows:

$$R_L = \frac{1}{1 + K_L C_0}. \quad (8)$$

If $0 < R_L < 1$, the adsorption course is advantageous adsorption; if $R_L = 1$, it is linear adsorption; if $R_L = 0$, it is nonreversible adsorption; if $R_L > 1$, it is unfavorable adsorption.[25,26]

The Freundlich model is an empirical model, which indicates that the adsorption process is multi-molecular layer adsorption. The nonlinear form of the Freundlich isotherm model (eqn (9)) can be expressed as follows:

$$q_e = kC_e^{1/n}, \quad (9)$$

where k is the Freundlich constant and n is the Freundlich constant indicating adsorption intensity.[27]

2.5.5 Evaluation of adsorption thermodynamics. The Gibbs equation and Van't Hoff isotherm were used to calculate the thermodynamic function of the reaction, and the Gibbs free energy change ΔG, enthalpy change ΔH and entropy change ΔS of BAC adsorption CV were obtained. The relevant calculation formula is as follows:

$$K_C = \frac{1000 K_L M_{adsorbate} C_{adsorbate}}{\gamma}, \quad (10)$$

$$\Delta G = -RT \ln K_C, \quad (11)$$

$$\Delta G = \Delta H - T\Delta S, \quad (12)$$

$$\ln K_C = -\frac{\Delta G}{RT} = \frac{\Delta S}{R} - \frac{\Delta H}{RT}, \quad (13)$$

where K_C represents the thermodynamic equilibrium constant, $M_{adsorbate}$ represents the molar mass of the adsorbed material, $C_{adsorbate}$ is the standard concentration of an adsorbed substance, γ represents the dimensionless activity coefficient, R is the gas constant, and the value is 8.314 J (mol^{-1} K^{-1}).

3 Results and discussion

3.1 Proximate analysis and elemental analysis of bamboo fiber

As shown in Table 2, bamboo fiber is a good clean raw material with a carbon content of 49.24%, high C/H and O/H, N content of less than 1%, and no S detected. The industrial analysis results showed that the volatile content of bamboo fiber was as high as 84.93% and the ash content as low as 2.21%, indicating that bamboo fiber was suitable for pyrolysis transformation.

Table 2 Proximate analysis and elemental analysis of bamboo fiber

Proximate analysis (wt%)				Elemental analysis (wt%)				
V_{ad}	FC_{ad}	A_{ad}	M_{ad}	C	H	N	O	S
84.93	11.69	2.21	1.17	49.24	6.66	0.42	43.69	—

3.2 The basic properties of bamboo fiber

TGA and FTIR are usually used as general methods to characterize the basic properties (pyrolysis behavior and basic functional groups) of raw biomass materials. The pyrolysis behavior and functional groups of bamboo fiber are shown in Fig. 1 and 2, respectively.

As shown in Fig. 3, the pyrolysis process of bamboo fiber (RC) can be divided into three stages. The first stage ranged from 21 °C to 76 °C attributed to the desorption of the water molecules on the surface of RC. The second pyrolysis stage was from 76 °C to 375 °C, which was attributed to the pyrolytic nature of cellulose. A pyrolytic temperature higher than 375 °C was the third stage, which was caused by the carbonization of involved lignin and cellulose. When the pyrolytic temperature was higher than 550 °C, the weight loss of RC was complete. In other words, the calculated temperature of 550 °C is a suitable temperature to obtain bamboo fiber carbon (the raw materials to prepare bamboo fiber-based activated carbon).

As presented in Fig. 4, there were obvious absorption peaks in the range of 750 cm^{-1} to 3700 cm^{-1}. The broad absorption peak at 3341 cm^{-1} was related to the hydroxyl (–OH) stretching vibration of alcohol and phenol molecules in bamboo fiber. The absorption peak at 2887 cm^{-1} was caused by the symmetric stretching vibration of methyl and methylene ($-CH_3$ and $-CH_2$). The characteristic absorption peak at 1593 cm^{-1} was attributed to the stretching vibration peak of lignin aromatic ring C=O. The absorption peaks at 1420 cm^{-1} and 1320 cm^{-1} correspond to the deformation vibration and bending vibration of aliphatic C–H on bamboo fiber polymers, respectively.

3.3 Optimization studies

3.3.1 Experimental results and analysis of variance. The response surface experimental factor levels and results are shown in Table 3.

The obtained data were statistically analyzed using Design-Expert 10.0.1 software. According to the experimental data, the final models are represented by the codes as follows:

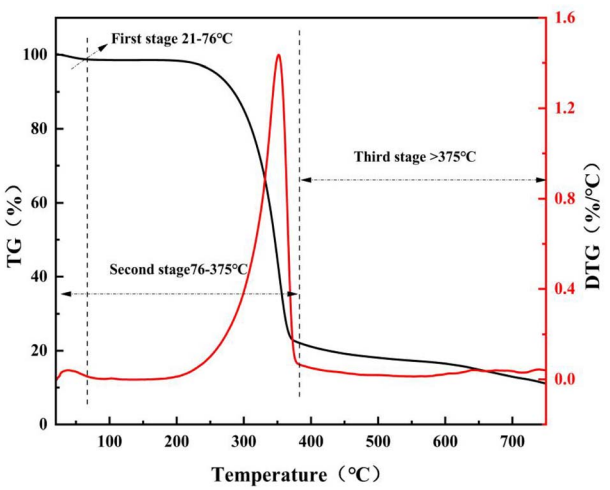

Fig. 3 Thermal weight loss curve of bamboo fiber powder.

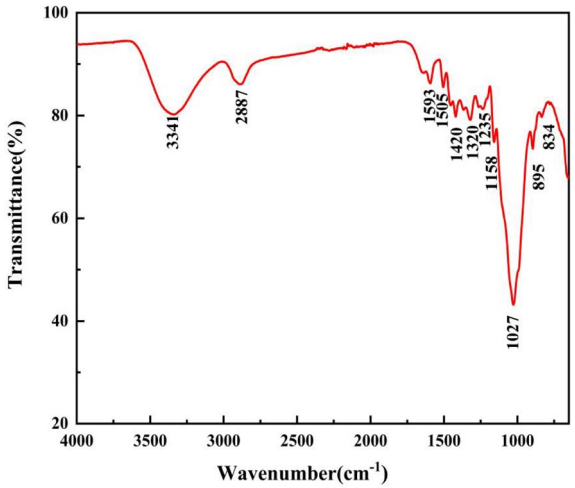

Fig. 4 FTIR spectra of bamboo fiber powder.

$$Y = 3732.78 + 66.8785A + 21.4625B - 33.3537C - 53.1837AB - 99.7535AC - 4.18015BC - 140.358A^2 - 47.1241B^2 - 203.451C^2.$$

The results of the ANOVA are given in Table 4. The F value can reflect the significance of the influence of the three variables on the iodine adsorption value.[28] The larger the F value, the higher the significance of the corresponding variable. The high values of R^2 (=0.9817) and $R_{adj}{}^2$ (=0.9581) indicate that the experimental model fits well with real data, which can provide theoretical and practical guidance for experimental optimization. A smaller lack of fit P (0.4490) value means that the specific model item contributes more to the response.[29,30]

3.3.2 3-D response surface analysis. Fig. 5 is the 3-dimensional surface plot and the contour diagram of the combined effects of the varied elements on BAC iodine adsorption value. We can see from Fig. 5(a) that the interaction of temperature A and time B has a parabolic distribution on the iodine adsorption value. When the temperature is constant, the iodine adsorption value increases and then decreases slightly as time increases. When time is constant, the iodine adsorption value increases and then decreases as the temperature increases. In contrast, temperature significantly affects iodine adsorption value than time. Setting the sensitive factor temperature A at 850–900 °C can significantly improve the iodine adsorption level.

Fig. 5(b) shows the interaction of temperature A and alkali–carbon ratio C with the iodine adsorption value. It can be observed from the plot that the temperature significantly affects the iodine adsorption value than the alkali–carbon ratio; take a moderate level: when temperature A is 850–875 °C and alkali/carbon ratio C is 4.5–5.0, the iodine adsorption value is the highest. Fig. 5(c) shows that the interaction between time B and alkali-carbon ratio C presents a typical arched surface distribution, and the alkali–carbon ratio is a sensitive factor affecting the iodine adsorption value. According to the software prediction results and experimental verification, the optimum adsorption factors obtained were temperature A of 864 °C, time B of 46 min,

Table 3 The 3-factor design matrix and experimental results

Serial number	Temperature A	Activation time B	Alkali/carbon ratio C	Iodine adsorption value/R (mg g^{-1})
1	0	0	0	3754.32
2	1	0	−1	3571.94
3	−1	0	1	3405.51
4	0	0	0	3731.35
5	0	−1	1	3441.45
6	0	0	0	3679.46
7	0	0	0	3757.44
8	−1	1	0	3543.59
9	1	0	1	3303.38
10	0	1	−1	3531.31
11	0	0	0	3741.32
12	1	−1	0	3653.37
13	0	1	1	3458.59
14	0	−1	−1	3497.46
15	1	1	0	3607.36
16	−1	0	−1	3275.05
17	−1	−1	0	3376.87

Table 4 Response surface fitting regression equation variance analysis results

Source	SS[a]	DF[b]	Mean square	F	P value	Significance
Model	3.888×10^5	9	43196.33	41.67	<0.0001	**
A – temperature	35781.87	1	35781.87	34.52	0.0006	**
B – activation time	3685.11	1	3685.11	3.56	0.1013	
C – alkali/carbon ratio	8899.75	1	8899.75	8.59	0.0220	*
AB	11314.03	1	11314.03	10.91	0.0131	*
AC	39803.06	1	39803.06	38.40	0.0004	**
BC	69.89	1	69.89	0.067	0.8026	
A^2	82949.33	1	82949.33	80.02	<0.0001	**
B^2	9350.24	1	9350.24	9.02	0.0198	*
C^2	1.743×10^5	1	1.743×10^5	168.13	<0.0001	**
Residual	7256.11	7	1036.59			
Lack of fit	3265.89	3	1088.63	1.09	0.4490	
Pure error	3990.23	4	997.56			
Total	3.960×10^5	16				

[a] Annotation: sum of squares. [b] Degree of freedom.

and alkali–carbon ratio C of 4.85 : 1. The activated carbon prepared under these optimal conditions was named BAC.

3.4 Characterization analysis of RC and BAC

3.4.1 Specific surface area and pore size distribution. Fig. 6(a) shows the N_2 adsorption and desorption isotherms of BAC and RC. According to the IUPAC classification rule, it is known that the N_2 adsorption and desorption isotherm of BAC belongs to the mixed type I and type VI.[31] At the initial stage of the adsorption process, N_2 adsorption capacity shows a trend of rapid increase, indicating that there are abundant micropores in BAC; with the increase of P/P_0, the adsorption curve gradually flattens; when P/P_0 was in the range of 0.4–0.9, there was a lagging loop, which is connected with capillary condensation that occurs in the mesoporous.[32]

As can be seen from the aperture distribution of BAC in Fig. 6(b), there are two peaks at 1.78 nm and 3.1 nm, indicating that micropores and mesopores occupy a large proportion, which is in line with the results obtained by the adsorption isotherm of BAC.

The specific surface area of activated carbon directly affects its adsorption rate. The general activated carbon specific surface area is between 500 m^2 g^{-1} and 1700 m^2 g^{-1}; the larger the specific surface area, the more favorable the adsorption process. Table 5 shows the BET-specific surface areas and pore-size distributions of the BAC and RC, respectively. It is clearly shown that BAC has a well-developed porous structure with a specific surface area of 2892 m^2 g^{-1}, which is much larger than that of RC (23.97 m^2 g^{-1}). The total pore volume of BAC is 1.796 cm^3 g^{-1}, and the proportion of the micropore volume is 26.45%. Therefore, BAC is mainly mesoporous. The results revealed that KOH activation played a momentous role in increasing the specific surface area of the BAC. As mentioned above, micropores offer an adsorption locus, and mesoporous pores determine the adsorption speed. Abundant

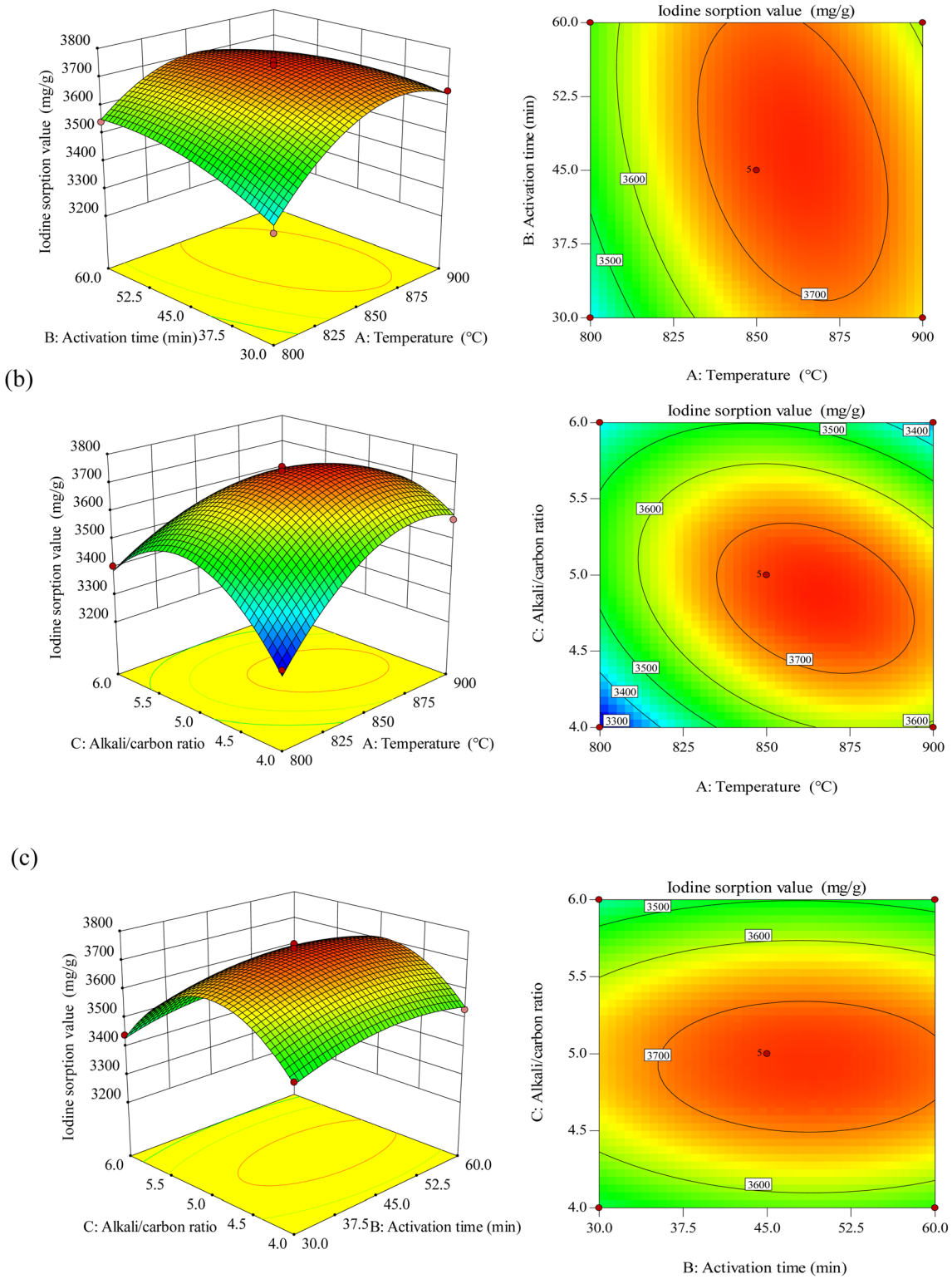

Fig. 5 Response surface plots for the influence of activation temperature and activation time (a), activation temperature and alkali/carbon ratio (b), activation time and alkali/carbon ratio (c).

mesoporous pores effectively enhance the adsorption capacity of BAC.

3.4.2 Morphology of RC and BAC. The surface morphology characteristics of RC and BAC are shown in Fig. 7. It can be seen from Fig. 7(a) and (b) that RC and BAC are fibrous in microscopic morphology, respectively. After activation, the structure of BAC was observed to be distorted and deformed, and the material presented a finer stick and block structure, indicating

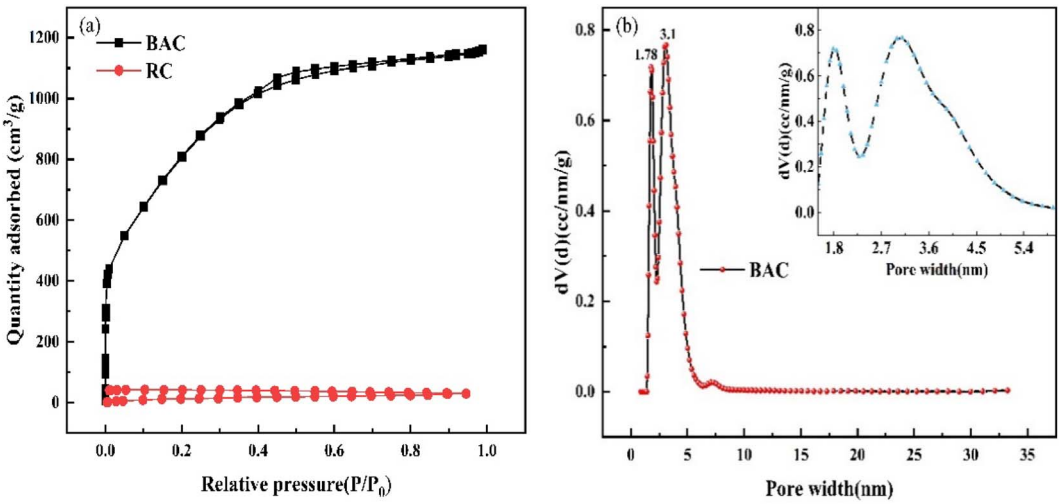

Fig. 6 N_2 adsorption and desorption isotherms (a) and pore size distributions of BAC (b).

Table 5 Specific surface area and pore structure of BAC

Samples	S_{BET} ($m^2\ g^{-1}$)	V_{mic} ($cm^3\ g^{-1}$)	V_{mes} ($cm^3\ g^{-1}$)	V_{total} ($cm^3\ g^{-1}$)	V_{mic}/V_{total} (%)	D_P (nm)
RC	23.97	0	0.04	0.04	0	7.08
BAC	2892	0.48	1.32	1.80	26.45	2.48

that the surface structure of the carbon material was destroyed under the etching action of KOH at high temperatures.[33,34] The undulating fold structure on the surface of activated carbon can effectively increase the contact area between it and the target pollutant. In the process of bamboo fiber pyrolysis, a large amount of organic matter volatilizes, and its asymmetric space shrinks, resulting in the formation of a carbon skeleton. As illustrated in Fig. 7(e) and (f), the basic pore structure of the bamboo fiber is maintained during carbonization and activation. Combined with the BET characterization results, activated carbon has many micropores and mesoporous structures that provide rich adsorption sites for bamboo fiber-activated carbon.

3.4.3 Carbon microcrystalline structure of RC and BAC. The XRD spectra of RC and BAC are shown in Fig. 8(a). The wide diffraction peak of RC at 22.5° corresponds to the (002) crystal plane of the graphite structure, which is a typical crystalline structure of cellulose. Some minerals, such as $CaCO_3$, were also detected in the RC. After KOH modification, the microcrystallinity and the graphitization degree of bamboo fiber-activated carbon decreased.[35]

The Raman spectra of RC and BAC are presented in Fig. 8(b). Peaks D and G were observed in the spectrograms of the two materials. Peak D indicates that the samples have amorphous C atoms with structural defects, which represents the characteristic peak of disordered carbon; peak G indicates that the C atom SP^2 of the sample is hybridized and represents the characteristic peak of ordered graphite structure.[36,37] The increase in the BAC peak intensity ratio (I_D/I_G) indicated that the aromatic structure with high stability increased; the activation process of KOH increased the structural defects of the activated carbon and deformed its carbon layer, which can effectively transport ions and improve the adsorption performance of the activated carbon.[38]

3.4.4 Elemental composition analyses of RC and BAC. The elemental composition of RC and BAC and the bonding forms of C, N and O were analyzed by X-ray photoelectron spectroscopy. It can be seen from Fig. 9(a) and (e) that RC consists mainly of C and O elements, with a small amount of N, Ga and Si elements. BAC consists mainly of C and O elements, with a small amount of N and Si elements. The high-resolution C 1s spectra of the two materials can be best fitted by five atomic states. In Fig. 9(b), there are four types of carbon atoms connected with N, O and Si in the C 1s spectrum of RC. The peak centered at 281.9 eV represents the C–Si, the peak centered at 283.5 eV corresponds to the C–C or C=C, the strong peak indicates that the bonding mode of C in RC is dominated by C=C, and the C element with SP^3 hybridization is the main body. The peak centered at 285.6 eV is C–O/C–N. The single peak at 287.9 eV indicates that C and O mainly exist in the form of double bonds; O 1s showed three obvious peaks at 529 eV, 530.7 eV and 532.2 eV in the energy spectrum, belonging to C=O, C–O–C and O–C=O, respectively. The N 1s spectrum shows two components, pyridinic-N and pyrrolic-N, located around 397.6 eV and 399.5 eV, respectively.

After activation, C content decreased from 88.50% to 88.32%, O content increased from 9.31% to 11.12%, and N content decreased to 0.35%. As depicted in the C 1s spectrum of BAC in Fig. 9(f), there are four peaks fitting at 282.2 eV, 284.3 eV, 285.7 eV and 288.4 eV, corresponding to C–Si, C–C/

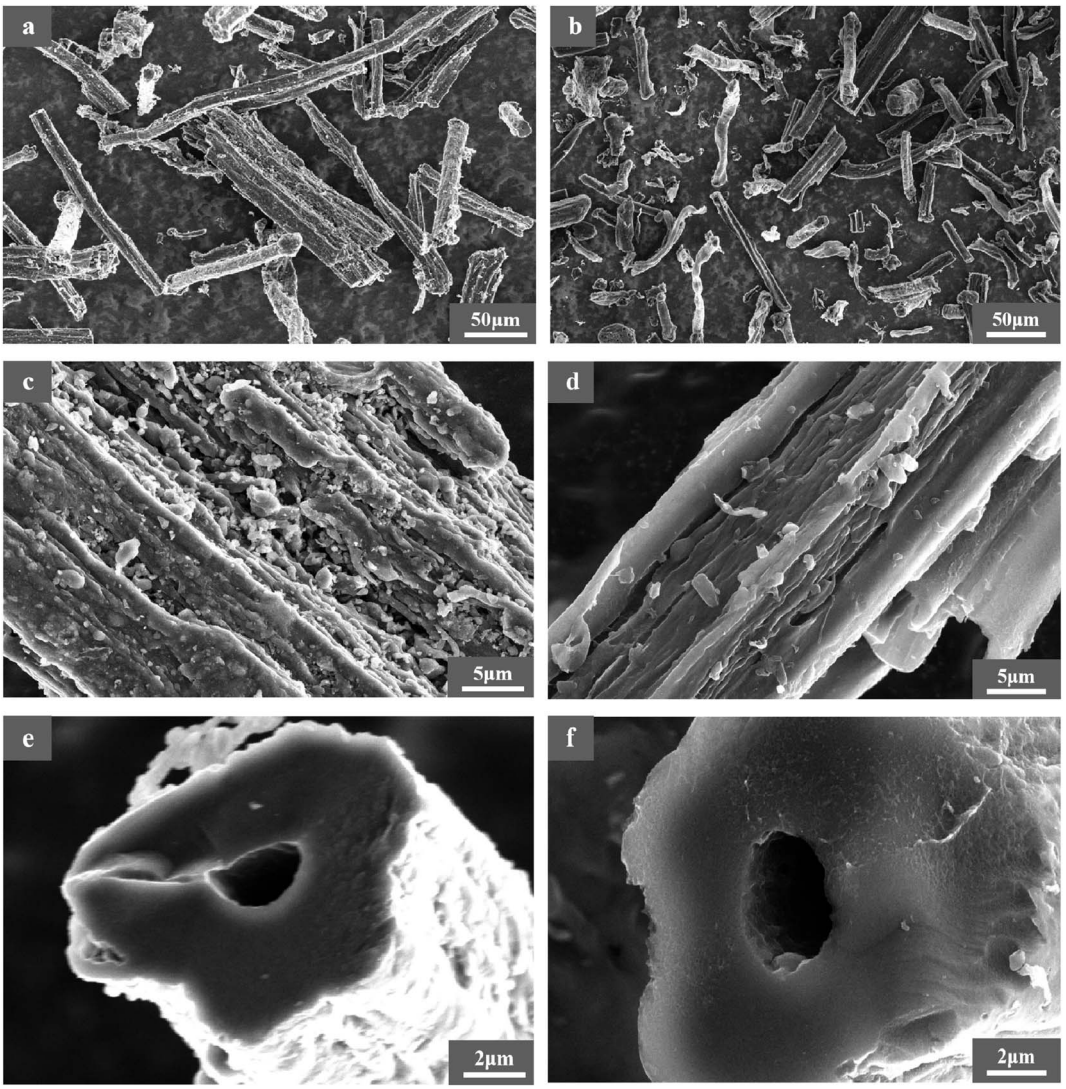

Fig. 7 Surface morphology of RC (a, c, and e) and BAC (b, d, and f).

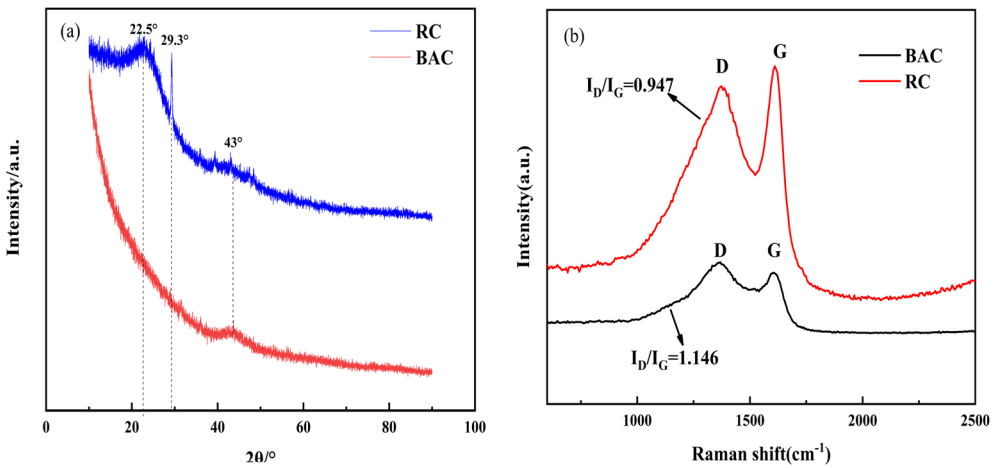

Fig. 8 XRD (a) and Raman (b) spectra of RC and BAC.

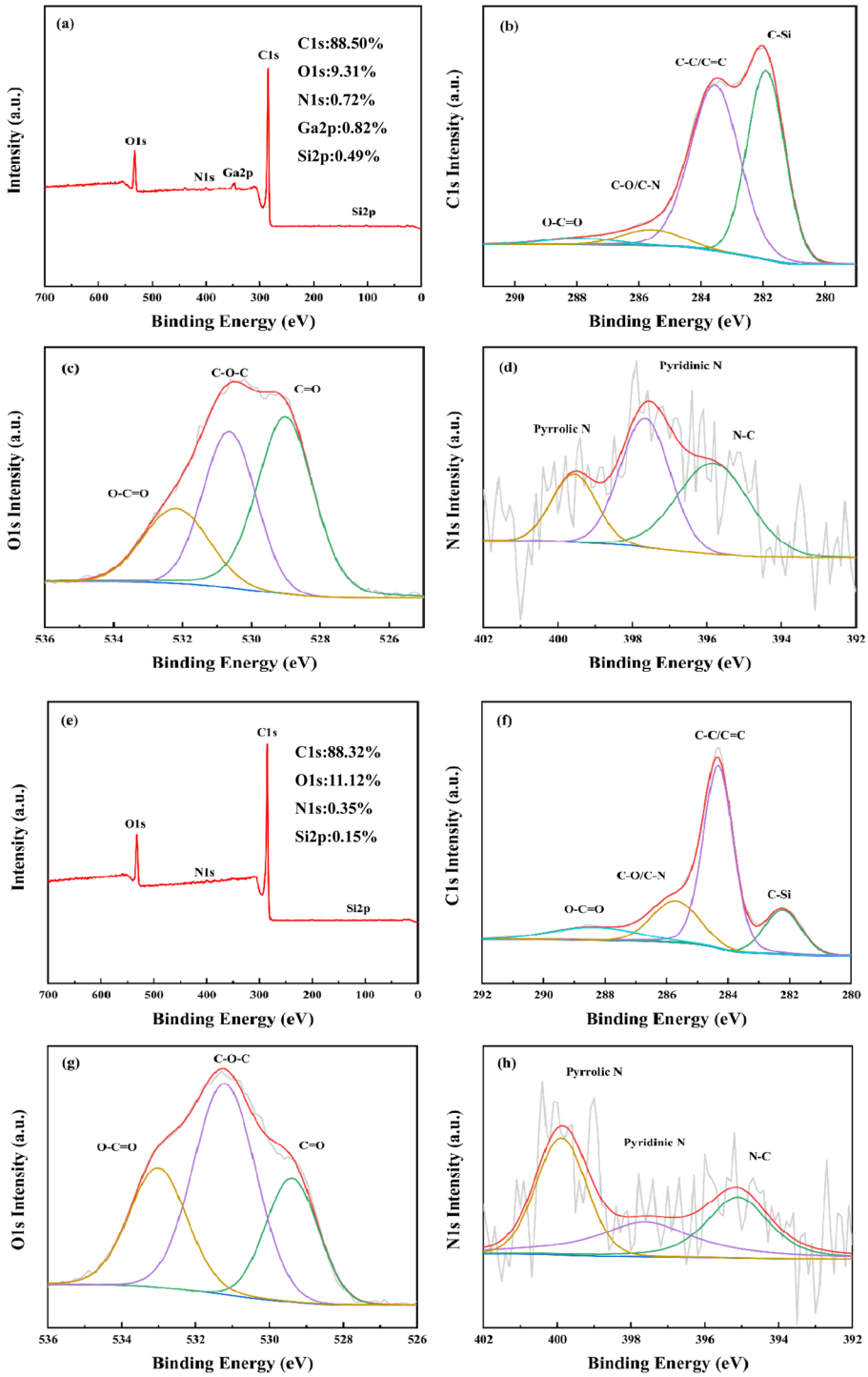

Fig. 9 X-ray photoelectron spectroscopy of RC (a–d) and BAC (e–h).

C═C, C–O/C═N and O–C═O, respectively. The three peaks at 529.4 eV, 531.3 eV and 533 eV in the O 1s spectrum represent C═O, C–O–C and O–C═O, respectively. Compared with O 1s in RC, carbon-based oxygen atoms in BAC produce higher binding energy at 533 eV.[39] The energy spectrum of N 1s shows that N in BAC mainly exists in the form of pyridinic-N and pyrrolic-N, which are located near 397.6 eV and 399.9 eV, respectively, followed by N–C located near 395.2 eV. The total amount of N and O elements is 11.47%, which is conducive to the hydrophilicity of BAC; BAC has a higher O 1s/C 1s atomic ratio. The results showed that KOH activation enriched the quantity of oxygen-containing functional groups on the surface of the activated carbon, which enhanced the polarity and acidity of the activated carbon surface. This property plays a positive role in promoting the adsorption of cationic dyes.

3.5 Adsorption experiment results

3.5.1 Effect of adsorbent dosage. Experiments were performed under the following conditions: temperature (298 K), rotational speed (120 rpm) and initial CV concentration (400 mg L^{-1}). As depicted in Fig. 10, when the dosage was increased from 0.01 g to 0.04 g, the CV removal rate increased to 100%. With the increase in BAC dosage, the total BAC-specific surface area and active adsorption site for adsorbing CV increased. The adsorption of CV leveled off gradually when the amount of BAC is enough. Simultaneously, it can be noticed that the unit mass adsorption capacity of BAC decreases gradually from 1717.435 mg L^{-1} to 332.687 mg L^{-1}. This may be because as the amount of BAC increases, carbon particles collide with each other, and the CV molecules surrounding BAC per unit mass are constantly reduced.[40,41] Therefore, the optimal dosage of 0.04 g was selected for subsequent experiments.

3.5.2 Effect of initial concentration. The impact of variation in the initial CV concentration from 400 mg L^{-1} to 900 mg L^{-1} was observed for adsorption (Fig. 11). The removal rate of CV by BAC decreased from 100% to 97.50%, and the adsorption capacity per unit mass increased from 499.863 mg g^{-1} to 1094.147 mg g^{-1}. When the BAC dosage is constant, the number of pores on its surface is constant, and the number of surface functional groups and the active locus is also fixed. In the lower concentration range, the concentration difference between solid and liquid increases as the original concentration of CV increases, thereby increasing the driving force for the diffusion of CV molecules to the BAC surface in solution. Most CV molecules are adsorbed at the active locus on the BAC surface. However, owing to the limited active locus available for adsorption on the BAC surface, as the concentration continues to increase, the activated carbon reaches saturation adsorption capacity, and the concentration of residual crystal violet in the solution increases, leading to a reduction in removal rate.[42] When the CV initial concentration is 600 mg L^{-1}, BAC can remove 99.96% of CV and has a high adsorption capacity per unit mass.

3.5.3 Effect of adsorption time. As shown in Fig. 12, under the condition that the BAC dose was 0.04 g and the initial CV concentration was 600 mg L^{-1}, CV in the solution could easily be removed by BAC. Within 10 min after the adsorption, the

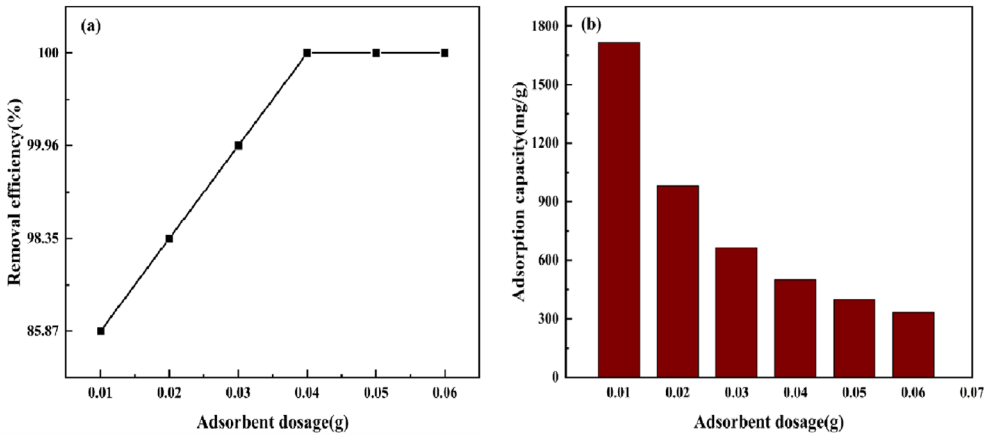

Fig. 10 Effect of adsorbent dosage on CV removal efficiency and adsorption capacity by BAC.

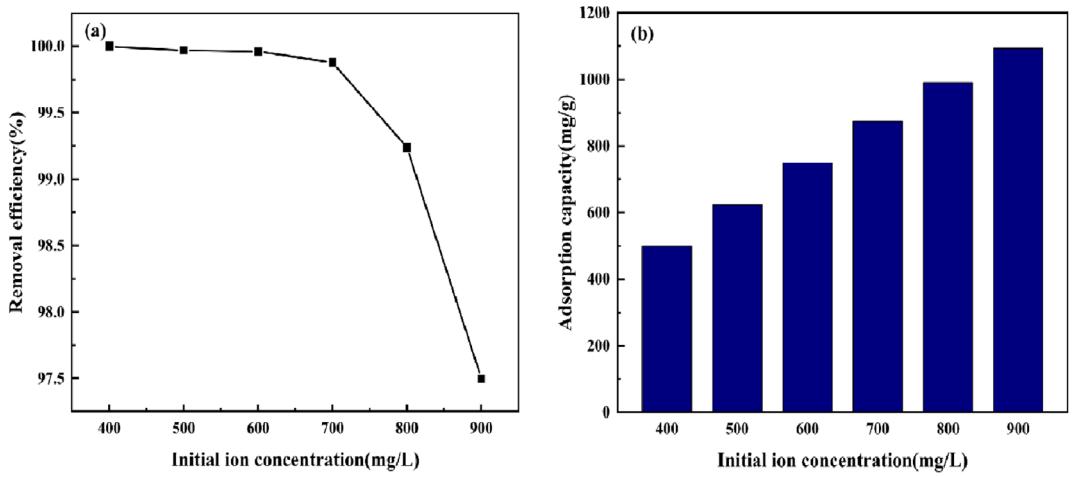

Fig. 11 The effect of initial concentration on CV removal efficiency and adsorption capacity.

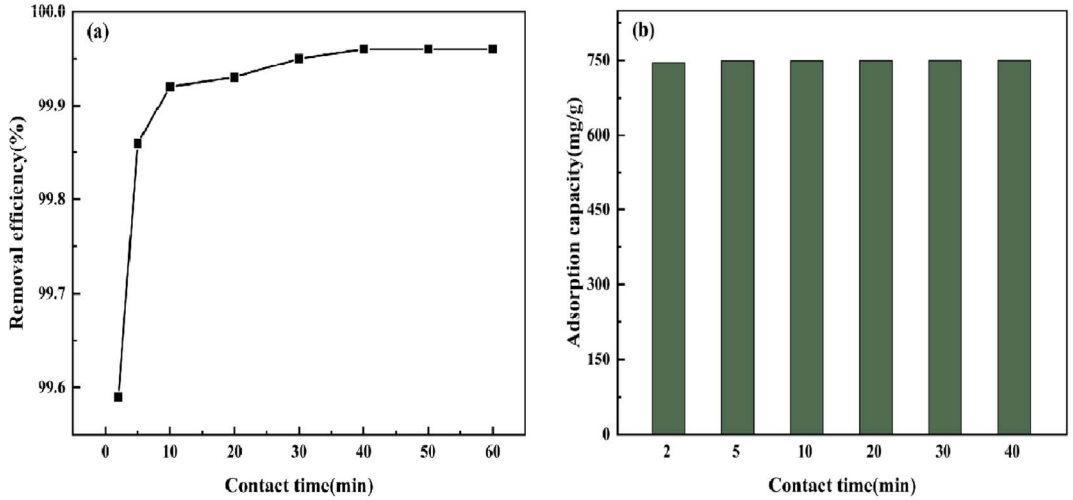

Fig. 12 The effect of contact time on CV removal efficiency and adsorption capacity.

removal rate reached 99.92%; this stage is the rapid adsorption stage. The following is a slow adsorption process in which the remaining CV molecules in the solution can only be allocated to the remaining low-activity adsorption sites on the BAC surface.[43] When the adsorption time is 40 min, the maximum adsorption capacity reaches 749.7 mg g^{-1}, and the reaction has reached the end point.

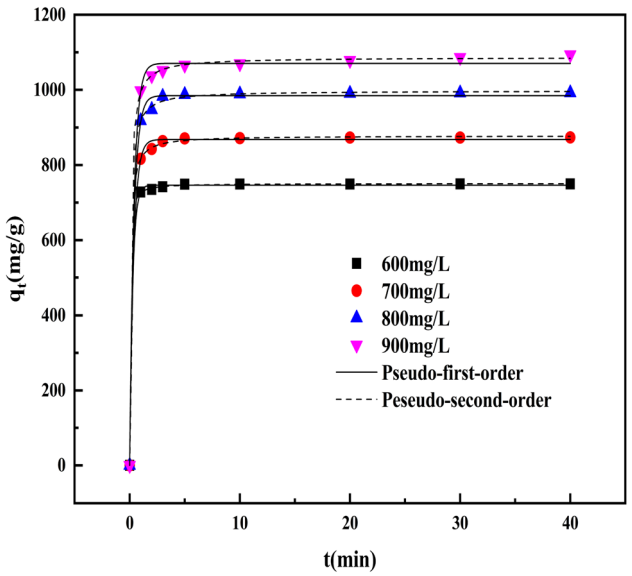

Fig. 13 Kinetics of CV adsorption onto BAC. (experimental conditions: temperature = 25 °C, dose = 0.04 g, agitation speed = 120 rpm, and volume = 50 mL).

3.5.4 Adsorption kinetics. Based on the adsorption kinetics, the adsorption mechanism of CV by BAC was predicted. The results of the kinetic model fitting are shown in Fig. 13 and Table 6. Through the calculation and comparison of regression coefficients (R^2) (Table 6), it can be concluded that the fitting R^2 values of the two models are close to 1. However, the R^2 value of the pseudo-second-order kinetic model is slightly higher than that of the pseudo-first-order kinetic model, and the calculated equilibrium adsorption capacity of the pseudo-second-order kinetic model is closer to the measured value. Therefore, adsorption is a process dominated by chemical adsorption and coexisted with physical adsorption.[44]

3.5.5 Adsorption isotherms. Fig. 14(a) and Table 7 demonstrate the adsorption isothermal model fitting curves and corresponding isotherm parameters, respectively. Comparing R^2 of the two models, the Langmuir isothermal model presents a very good fit, indicating that the CV adsorbed onto the homogeneous surface of BAC occurs in a monolayer. The maximum monolayer adsorption capacity (q_m) of BAC was estimated to be 1353.09 mg g^{-1}. The separation factors R_L are found between 0 and 1; it is proved that the adsorption process is favorable.[45] Freundlich constant n values are all greater than 2, indicating that BAC has a strong adsorption capacity.

Table 6 Kinetic parameters for adsorption of CV onto BAC

CV concentration (mg L^{-1})	Pseudo-first-order			Pseudo-second-order		
	k_1	q_e (mg g^{-1})	R^2	k_2	q_e (mg g^{-1})	R^2
600	3.68	746.51	0.99958	0.04	750.90	0.9999
700	2.77	868.15	0.99896	0.02	878.27	0.9998
800	2.64	984.24	0.9984	0.01	997.32	0.9996
900	2.63	1070.35	0.99776	0.01	1086.45	0.9998

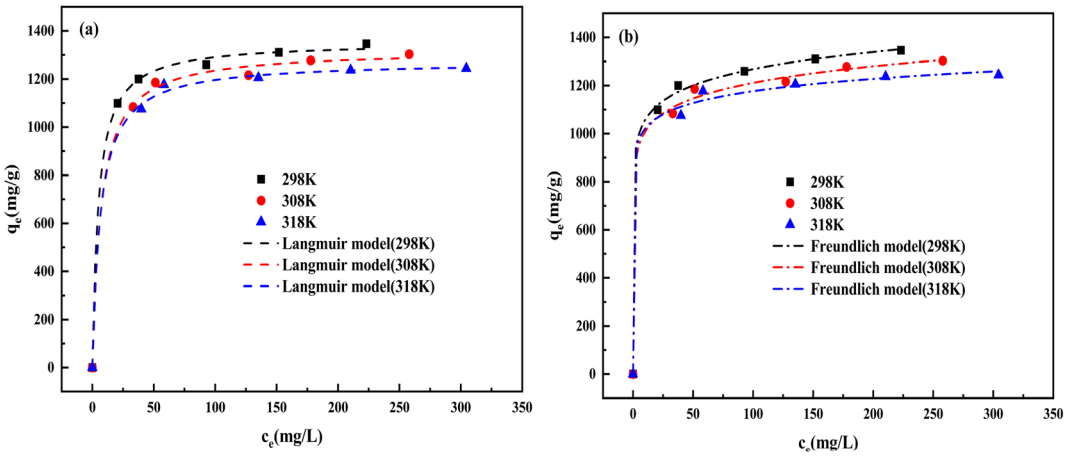

Fig. 14 (a) Langmuir isotherm model and (b) Freundlich isotherm model for CV adsorption on BAC.

Table 7 Isotherm parameters for CV adsorption

		Langmuir model			Freundlich model		
T (K)	q_{max} (mg g^{-1})	K_L	R_L	R^2	K_F	n	R^2
298	1353.09	0.21	0.0053	0.9989	886.68	12.67	0.9899
308	1321.05	0.14	0.0079	0.9978	839.43	12.56	0.9975
318	1274.44	0.15	0.0074	0.9985	886.69	16.28	0.9967

According to the results of the Langmuir fitting, the adsorption amount decreased significantly as the temperature increased, indicating that the increase in temperature was not conducive to the adsorption of BAC. It can be observed from Table 8 that, compared with other adsorbents, BAC has an outstanding ability to adsorb CV.

3.5.6 Thermodynamics studies. From Table 9, the thermodynamic arguments (ΔH, ΔS and ΔG) for CV adsorption on BAC were evaluated using the thermodynamic eqn (9)–(12). The negative value of enthalpy change ΔH (−13.45 kJ mol^{-1}) indicates that the adsorption process is exothermic, which agrees with the changing trend of the maximum theoretical equilibrium adsorption capacity in the parameter table.[51] The entropy change (ΔS) was positive, indicating that adsorption is a process of entropy increase that reflects the random increase in the reaction interface between CV and BAC during the adsorption process. ΔG was negative, indicating that the adsorption reaction is an autonomous process driven by entropy.

3.5.7 SEM-EDS analysis before and after BAC adsorption. As shown in Fig. 15, by comparing the scanning electron microscope images before and after BAC adsorption, it can be found that after the adsorption of CV, obvious white particles and bright areas appeared on the surface of the BAC. It is speculated that the adsorption process includes precipitation, which results in the enrichment of CV on the BAC surface.[52] Fine particles can be seen around and inside the pores, indicating that the adsorption process also involves pore filling. As can be seen from the EDS spectrum of BAC in Fig. 15(a), its C content is the highest, in addition to some O and N. After the adsorption of CV, C content increased to 98.71%, N content increased from 0.59% to 0.96%, and O content decreased from 3.13% to 0.02%. The decrease in the O element indicated that the oxygen-containing functional groups on the BAC surface react with CV during the adsorption process. N bonded with oxygen-containing functional groups through bond energy, speeding up the adsorption

Table 9 Thermodynamic parameters for CV adsorption onto BAC

T (K)	ΔG (kJ mol^{-1})	ΔH (kJ mol^{-1})	ΔS (kJ mol^{-1} K^{-1})
298	−28.14	−13.45	0.048
308	−28.05		
318	−28.14		

Table 8 Comparison of CV removal ability of different adsorbents

Material	Initial concentration/mg L^{-1}	Adsorption dose/mg	Time/min	pH	Temperature/°C	Adsorption capacity/mg g^{-1}	References
Modified rice husk	1000	25	60	10	25	90.02	46
Chitin activated carbon	500	50	80	10	45	420.068	47
Coconut husk powder	500	250	150	5	45	454.54	48
Pomegranate peel charcoal	40.1	79	5.7	9.9	25	211.8	49
Cocoa leaves biochar	100	400	160	9	27	253.3	50
BAC	900	40	90	7	25	1099.036	This work

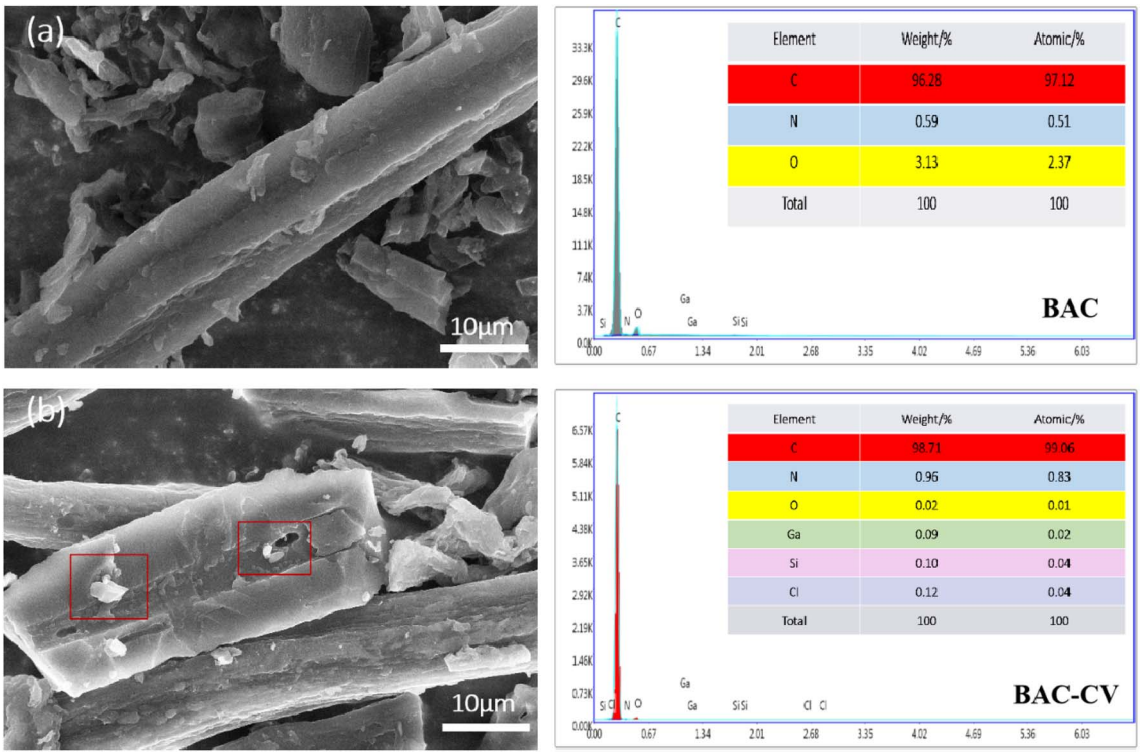

Fig. 15 SEM-EDS images before (a) and after (b) adsorption of the dye on BAC.

reaction. It can be concluded that ionic action and oxygen-containing functional groups played an important role in promoting the adsorption process.

4 Conclusion

In this study, the adsorption of CV from aqueous solutions using the BAC adsorbent prepared from the bamboo fiber was investigated. Various analyses, such as BET, SEM, XRD, Raman and XPS, were performed and used to study the surface properties of the BAC. According to the experimental results, the adsorption efficiency and adsorption capacity of BAC were found to be influenced by several factors (adsorbent dosage, initial CV concentration and contact time). The adsorption process of CV on BAC is more consistent with the pseudo-second-order kinetic model and Langmuir isothermal model, indicating that CV adsorbed onto the homogeneous surface of BAC occurs in a monolayer. The thermodynamic investigations showed that the adsorption processes were feasible and spontaneous. The maximum adsorption capacity of BAC on CV reached up to 1353.09 mg g^{-1}. By analyzing the changes in the types and contents of micro-elements on the BAC surface before and after adsorption, CV was successfully adsorbed; ion exchange and oxygen-containing functional groups provided an important driving force for the adsorption process. It is noteworthy that if the adsorbed saturated activated carbon is not regenerated, it causes secondary pollution to the environment. Therefore, the next step of this study will focus on the reuse of activated carbon.

Conflicts of interest

The authors declare that there is no conflict of interest regarding the publication of this paper.

Acknowledgements

This work was partially supported by the National Natural Science Foundation of China (22208138), the Nature Science Foundation of Liaoning Province (2021-MS-306), Liaoning Provincial Department of Education Project (2020LNQN03).

References

1 L. J. J. Isotherm, Kinetic, Thermodynamic and Competitive for Adsorption of Brilliant Green and Quinoline Yellow Dyes by Activated Carbon, *Korean Chem. Eng. Res.*, 2021, **59**(4), 565–573.
2 A. M. Aldawsari, I. H. Alsohaimi, A. A. Kahtani, *et al.*, Adsorptive performance of aminoterephthalic acid modified oxidized activated carbon for malachite green dye: mechanism, kinetic and thermodynamic studies, *Sep. Sci. Technol.*, 2021, **56**(5), 835–846.
3 Y. F. Zeng, J. Liu, J. X. Qiu, *et al.*, Research Progress in Electrochemical Methods for Treatment of Heavy Metal Electroplating Wastewater, *Recycling Research*, 2018, **11**(6), 42–44.
4 L. Mahardiani, R. Ilfama, S. Saputro, *et al.*, Nanocellulose Obtained from Biomass as Advance Adsorbent for

Methylene Blue and Crystal Violet, *J. Phys.: Conf. Ser.*, 2021, **1912**(1), 12015.

5 G. Sangavi, A. Bakshi, M. Ganapathy, *et al.*, Adsorption of Reactive Dyes from Aqueous Solution Using Activated Carbon Prepared from Plantain Leaf Sheath Waste, *Chem. Biochem. Eng. Q.*, 2020, **34**(3), 169–180.

6 S. A. Nisreen, R. K. Khairi, N. A. Amer, *et al.*, Albayati Performance of a solar photocatalysis reactor as pretreatment for wastewater via UV, UV/TiO_2, and UV/H_2O_2 to control membrane fouling, *Sci. Rep.*, 2022, **12**, 16782.

7 Y. Laftani, A. Boussaoud, B. Chatib, *et al.*, Comparison of advanced oxidation processes for degrading Ponceau S dye. Application of photo-Fenton process, *Maced. J. Chem. Chem. Eng.*, 2019, **38**(2), 197–205.

8 J. Wang, X. Yang, D. Y. Zheng, *et al.*, Fabrication of Bioinspired Gallic Acid-Grafted Chitosan/Polysulfone Composite Membranes for Dye Removal via Nanofiltration, *ACS Omega*, 2020, **5**(22), 13077–13086.

9 L. Aoudjit, D. Zioui, F. Touahra, *et al.*, Photocatalytic Degradation of Tartrazine Dyes Using TiO2–Chitosan Beads under Sun Light Irradiation, *Russ. J. Phys. Chem. A*, 2021, **95**(5), 1069–1076.

10 S. Singh, A. K. Prajapati, J. P. Chakraborty, *et al.*, Adsorption Potential of Biochar Obtained from Pyrolysis of Raw and Torrefied Acacia Nilotica Towards Removal of Methylene Blue Dye from Synthetic Wastewater, *Biomass Convers. Biorefin.*, 2021, 1–22.

11 L. D. Li, S. Y. Tan, W. P. Su, *et al.*, Research Progress of Crystal Violet Dyeing Wastewater Treatment Technology, *Environ. Sci. Technol.*, 2017, **40**(S2), 179–183.

12 Y. Laftani, A. Boussaoud, B. Chatib, *et al.*, Comparison of Advanced Oxidation Processes for Degrading Ponceau S Dye. Application of Photo-Fenton Process, *Maced. J. Chem. Chem. Eng.*, 2019, **38**(2), 197–205.

13 Y. Chen, N. Cheng, Y. B. Yang, *et al.*, Adsorption of Crystal Violet Dye by Physical Ultrasonic Modified Bentonite, *Ind. Water Treat.*, 2021, **41**(09), 98–103.

14 D. N. C. Brice, N. H. Manga, B. S. Arnold, *et al.*, Adsorption of Tartrazine onto Activated Carbon Based Cola Nuts Shells: Equilibrium, Kinetics, and Thermodynamics Studies, *Open J. Inorg. Chem.*, 2021, **11**(01), 1–19.

15 W. Dai, H. Yu, N. Ma, *et al.*, Adsorption Equilibrium and Kinetic Studies of Crystal Violet and Naphthol Green on Torreya-Grandis-Skin-Based Activated Carbon, *Korean J. Chem. Eng.*, 2015, **32**(2), 335–341.

16 H. Zhang, Y. Sun, S. Li, *et al.*, Preparation, Characterization, and Efficient Chromium (Vi) Adsorption of Phosphoric Acid Activated Carbon from Furfural Residue: An Industrial Waste, *Water Sci. Technol.*, 2020, **82**(12), 2864–2876.

17 A. Ghazali, M. Shirani, A. Semnani, *et al.*, Optimization of Crystal Violet Adsorption onto Date Palm Leaves as a Potent Biosorbent From Aqueous Solutions Using Response Surface Methodology and Ant Colony, *J. Environ. Chem. Eng.*, 2018, **6**(4), 3942–3950.

18 B. G. Salas-Enríquez, A. M. Torres-Huerta, E. Conde-Barajas, *et al.*, Activated carbon production from the Guadua amplexifolia using a combination of physical and chemical activation, *J. Therm. Anal. Calorim.*, 2016, **124**(3), 1383–1398.

19 X. L. Hou, Q. Guo, X. P. Jian, *et al.*, Optimization of Design of Lignin-Based Activated Carbon Based on Response Surface Methodology, *Chem. Ind. For. Prod.*, 2020, **40**(03), 115–122.

20 C. Tian and D. Wu, Mechanical Properties of ZSM-5 Extruded Catalysts: Calcination Process Optimization Using Response Surface Methodology, *Chem. Eng. Commun.*, 2021, **208**(11), 1594–1606.

21 O. Oribayo, A. P. Olalekan, R. U. Owolabi, *et al.*, Adsorption of Cr(Vi) Ions From Aqueous Solution Using Rice Husk-Based Activated Carbon: Optimization, Kinetic, and Thermodynamic Studies, *Environmental Quality Management*, 2020, **30**(1), 61–77.

22 W. Wang, Y. Liu, X. Liu, *et al.*, Equilibrium Adsorption Study of the Adsorptive Removal of Cd^{2+} and Cr^{6+} Using Activated Carbon, *Environ. Sci. Pollut. Res.*, 2018, **25**(25), 25538–25550.

23 S. M. Kharrazi, M. Soleimani, M. Jokar, *et al.*, Pretreatment of Lignocellulosic Waste as a Precursor for Synthesis of High Porous Activated Carbon and its Application for Pb (Ii) and Cr(Vi) Adsorption from Aqueous Solutions, *Int. J. Biol. Macromol.*, 2021, **180**, 299–310.

24 G. K. Latinwo, A. O. Alade, S. E. Agarry, *et al.*, Process Optimization and Modeling the Adsorption of Polycyclic Aromatic-Congo Red Dye onto Pod-Derived Activated Carbon, *Polycyclic Aromat. Compd.*, 2021, **41**(2), 400–418.

25 T. V. Nagalakshmi, K. A. Emmanuel and P. Bhavani, Adsorption of Disperse Blue 14 onto Activated Carbon Prepared from Jackfruit-Ppi-I Waste, *Mater. Today: Proc.*, 2019, **18**(6), 2036–2051.

26 A. Kumar and H. M. Jena, Adsorption of Cr(Vi) From Aqueous Solution by Prepared High Surface Area Activated Carbon From Fox Nutshell by Chemical Activation with H_3Po_4, *J. Environ. Chem. Eng.*, 2017, **5**(2), 2032–2041.

27 A. Lim, J. J. Chew, L. H. Ngu, *et al.*, Synthesis, Characterization, Adsorption Isotherm, and Kinetic Study of Oil Palm Trunk-Derived Activated Carbon for Tannin Removal from Aqueous Solution, *ACS Omega*, 2020, **5**(44), 28673–28683.

28 L. Brahmi, F. Kaouah, S. Boumaza, *et al.*, Response Surface Methodology for the Optimization of Acid Dye Adsorption onto Activated Carbon Prepared from Wild Date Stones, *Appl. Water Sci.*, 2019, **9**(8), 1–13.

29 A. Dzigbor and A. Chimphango, Production and Optimization of NaCl-Activated Carbon from Mango Seed Using Response Surface Methodology, *Biomass Convers. Biorefin.*, 2019, **9**(2), 421–431.

30 O. Baytar, Ö. Şahin, S. Horoz, *et al.*, High-Performance Gas-Phase Adsorption of Benzene and Toluene on Activated Carbon: Response Surface Optimization, Reusability, Equilibrium, Kinetic, and Competitive Adsorption Studies, *Environ. Sci. Pollut. Res.*, 2020, **27**(21), 26191–26210.

31 M. Şirazi and S. Aslan, Comprehensive Characterization of High Surface Area Activated Carbon Prepared from Olive Pomace by Koh Activation, *Chem. Eng. Commun.*, 2021, **208**(10), 1479–1493.

32 C. Tian and D. Wu, Mechanical Properties of ZSM-5 Extruded Catalysts: Calcination Process Optimization Using Response Surface Methodology, *Chem. Eng. Commun.*, 2021, **208**(11), 1594–1606.
33 A. H. Jawad, A. S. Abdulhameed, N. N. Bahrudin, *et al.*, Microporous activated carbon developed from KOH activated biomass waste: surface mechanistic study of methylene blue dye adsorption, *Water Sci. Technol.*, 2021, **84**(8), 1858–1872.
34 A. Jawad, S. Ahmed, D. Lee, *et al.*, High surface area and mesoporous activated carbon from KOH-activated dragon fruit peels for methylene blue dye adsorption: Optimization and mechanism study, *Chin. J. Chem. Eng.*, 2021, **32**(04), 281–290.
35 G. Kavitha, P. Subhapriya, V. Dhanapal, *et al.*, Dye Removal Kinetics and Adsorption Studies of Activated Carbon Derived from the Stems of Phyllanthus Reticulatus, *Mater. Today: Proc.*, 2021, **45**(9), 7934–7938.
36 D. Bal Altuntaş, V. Nevruzoğlu, M. Dokumacı, *et al.*, Synthesis and Characterization of Activated Carbon Produced from Waste Human Hair Mass Using Chemical Activation, *Carbon Lett.*, 2020, **30**(3), 307–313.
37 V. Dodevski, B. Janković, I. Radović, *et al.*, Characterization Analysis of Activated Carbon Derived from the Carbonization Process of Plane Tree (Platanus Orientalis) Seeds, *Energy Environ.*, 2020, **31**(4), 583–612.
38 M. Gale, T. Nguyen, M. Moreno, *et al.*, Physiochemical Properties of Biochar and Activated Carbon from Biomass Residue: Influence of Process Conditions to Adsorbent Properties, *ACS Omega*, 2021, **6**(15), 10224–10233.
39 L. Liu, Y. Li and S. Fan, Preparation of Koh and H_3Po_4 Modified Biochar and its Application in Methylene Blue Removal from Aqueous Solution, *Processes*, 2019, **7**(12), 891.
40 R. Foroutan, S. J. Peighambardoust, S. H. Peighambardoust, *et al.*, Adsorption of Crystal Violet Dye Using Activated Carbon of Lemon Wood and Activated Carbon/Fe_3O_4 Magnetic Nanocomposite from Aqueous Solutions: A Kinetic, Equilibrium and Thermodynamic Study, *Molecules*, 2021, **26**(8), 2241.
41 B. Nba, B. Mf, B. So, *et al.*, Comparative Study on Removal of Two Basic Dyes in Aqueous Medium by Adsorption Using Activated Carbon from Ziziphus Lotus Stones - Sciencedirect, *Microchem. J.*, 2019, **146**, 1010–1018.
42 R. Nazir, M. Khan, R. Ur Rehman, *et al.*, Adsorption of Selected Azo Dyes from an Aqueous Solution by Activated Carbon Derived from Monotheca Buxifolia Waste Seeds, *Soil Water Res.*, 2020, **15**(3), 166–172.
43 F. P. Sari, D. H. Y. Yanto and G. Pari, Activated Carbon Derived from OPEFB by One Step Steam Activation and its Application for Dye Adsorption: Kinetics and Isothermal Studies, *Reaktor*, 2019, **19**(2), 68–76.
44 Y. Hou, G. Huang, J. Li, *et al.*, Hydrothermal Conversion of Bamboo Shoot Shell to Biochar: Preliminary Studies of Adsorption Equilibrium and Kinetics for Rhodamine B Removal, *J. Anal. Appl. Pyrolysis*, 2019, **143**, 104694.
45 G. K. Latinwo, A. O. Alade, S. E. Agarry, *et al.*, Process Optimization and Modeling the Adsorption of Polycyclic Aromatic-Congo Red Dye Onto; Pod-Derived Activated Carbon, *Polycyclic Aromat. Compd.*, 2021, **41**(2), 400–418.
46 H. P. Lal, P. Rachana, P. Sujan, *et al.*, Adsorption and removal of crystal violet dye from aqueous solution by modified rice husk, *Heliyon*, 2022, **8**(4), 9261.
47 Q. S. Ji and H. C. Li, High surface area activated carbon derived from chitin for efficient adsorption of Crystal Violet, *Diamond Relat. Mater.*, 2021, **118**, 108516.
48 S. Sharmin, I. Khairul, M. Hasan, *et al.*, Adsorption of crystal violet dye by coconut husk powder: Isotherm, kinetics and thermodynamics perspectives, *Environ. Nanotechnol., Monit. Manage.*, 2022, **17**, 100651.
49 S. Aiman, A. A. Saud, A. H. Jawad, *et al.*, Production of large surface area activated carbon from a mixture of carrot juice pulp and pomegranate peel using microwave radiation-assisted $ZnCl_2$ activation: An optimized removal process and tailored adsorption mechanism of crystal violet dye, *Diamond Relat. Mater.*, 2022, **130**, 109456.
50 J. J. Mosebolatan, A. M. Ayorinde, O. I. Adekunle, *et al.*, Synthesis of high surface area mesoporous ZnCl2–activated cocoa (Theobroma cacao L) leaves biochar derived via pyrolysis for crystal violet dye removal, *Heliyon*, 2022, **8**(10), 10873.
51 J. J. Lee and J. K. Jeon, Isotherm, Kinetic and Thermodynamic Studies on Adsorption of Bromocresol Purple, Acid Red 66 and Acid Blue 40 Using Activated Carbon, *J. Nanosci. Nanotechnol.*, 2021, **21**(7), 4104–4109.
52 J. A. Barbosa, G. Labuto and E. N. V. M. Carrilho, Magnetic Nanomodified Activated Carbon: Characterization and Use for Organic Acids Sorption in Aqueous Medium, *Chem. Eng. Commun.*, 2021, **208**(10), 1450–1463.